

Fabrication of an oxide/metal/oxide structured electrode integrated with antireflective film to enhance performance in flexible organic light-emitting diodes

K.-J. Ko ^{a, d}, S.-R. Shin ^{a, d}, H.B. Lee ^a, E. Jeong ^b, Y.J. Yoo ^c, H.M. Kim ^c, Y.M. Song ^{c, **}, J. Yun ^{b, ***}, J.-W. Kang ^{a, *}

^a Department of Flexible and Printable Electronics, LANL-CBNU Engineering Institute-Korea, Jeonbuk National University, Jeonju 54896, Republic of Korea

^b Surface Technology Division, Korea Institute of Materials Science, Changwon, Gyeongnam 51508, Republic of Korea

^c School of Electrical Engineering and Computer Science, Gwangju Institute of Science and Technology, Gwangju 61005, Republic of Korea

ARTICLE INFO

Article history:

Received 27 December 2020

Received in revised form

14 February 2021

Accepted 4 March 2021

Available online 9 March 2021

Keywords:

Light extraction

Silica nanoparticles

Refractive index

OMO TCE

Flexible OLED

ABSTRACT

Flexible organic light-emitting diodes (OLEDs) are used widely in optoelectronic devices, with possible new applications, including foldable/rollable displays. Unique features of flexible OLEDs included high brightness, low power consumption, and flexibility. The performance of a flexible OLED is frequently hindered by refractive index difference between the air and the flexible substrate medium, leading to inefficient light outcoupling. To address this issue, we developed a mechanically robust oxide/metal/oxide (OMO) structured transparent conducting electrode (TCE), integrated with silica nanoparticles-based antireflective (AR) film, to improve the light extraction efficiency of flexible OLEDs. The AR-OMO structures were prepared on polyethylene terephthalate substrates using a combination of plasma-enhanced chemical vapor deposition and magnetron sputtering. Our results show that an OLED device based on AR-OMO TCE exhibits higher luminance efficiency (*LE*) and total external quantum efficiency (*EQE_{tot}*) than devices based on pristine OMO or an indium tin oxide structure due to the presence of AR film that suppresses waveguided-mode light loss at the air-substrate interface. The champion AR-OMO-based flexible OLED devices achieved an *LE* of 12.3 cd/A and an *EQE_{tot}* of 5.0%. The AR-OMO device also demonstrated outstanding mechanical flexibility, retaining 100% of its initial luminance up to a bending radius of 6 mm.

© 2021 Elsevier Ltd. All rights reserved.

1. Introduction

Organic light-emitting diodes (OLEDs) have emerged as a next-generation display technology because of their high brightness, fuller viewing angle, wide color range, rapid refresh rates, and low power consumption. Furthermore, OLEDs have a simple design that is compatible with ultrathin, flexible, foldable, and transparent displays [1,2]. The overall performance and flexibility of OLED devices are governed by the optoelectronic properties of their transparent conductive electrodes (TCEs). Indium tin oxide (ITO), which

can be vapor-phase deposited on rigid or flexible substrates, is the most popular TCE material in many flexible optoelectronic devices because of its balanced optical transmittance-sheet resistance tradeoff. However, inherent brittleness, scarcity of indium, and non-vacuum-free manufacturing process have limited the application of ITO in flexible OLED devices [3]. Various ITO-free alternatives such as metal grid and nanowires (NWs) [2,4–9], carbon nanotube (CNT) [10–12], graphene [13–15], conductive polymers [16,17], and oxide/metal/oxide (OMO) structures [18–20] have evaluated as replacements for ITO in the fabrication flexible OLEDs. Each candidate has notable weaknesses to be universally accepted as the promising electrode candidate. For example, graphene reveals non-negligible disadvantages mainly because of the high degree of technical difficulty associated with large-area and high-throughput fabrication [21], whereas CNTs and PEDOT:PSSs are often excluded from consideration for high-performance optoelectronic applications because of their inferior optical

* Corresponding author.

** Corresponding author.

*** Corresponding author.

E-mail addresses: ymsong@gist.ac.kr (Y.M. Song), Jungheum@kims.re.kr (J. Yun), jwkwang@jbnu.ac.kr (J.-W. Kang).

^d K.-J. K. and S.-R.S. made equal contribution to this article.

transmittances [2]. The irregular, three-dimensional stacking structure of Ag NWs, which disrupts any sealing from an ambient environment, inevitably causes reliability issues owing to serious oxidation and thermal degradation [22]. Contrastively, OMO nanocomposite structures with an ultrathin noble metal film sandwiched between oxide layers such as ITO/Ag/ITO [23], WO₃/Ag/WO₃ [24], and ZnO/Ag/ZnO [19] are compatible with flexible OLED application. The unique structural configuration of OMO electrodes successfully circumvents the aforementioned restrictions. The OMO electrodes ensure superior chemical and structural stabilities against corrosion and thermal loads along with their competitive optoelectrical properties. The mechanical flexibility and scalability of OMOs for continuous, large-area, high-throughput fabrication using roll-to-roll coaters add the merit of OMOs as promising ITO alternatives.

However, the actual practice of OMO electrodes is still limited mainly by the inferior optical transmittance compared with crystalline ITO or Ag NWs. The serious reduction in the optical transmittance is an inevitable consequence of the increased thickness of the metal layer in the OMO configuration, which are required to attain a competitive electrical conductivity. This optical loss is inherent in metal layers because an increased thickness provides more chances of photon scattering owing to the interaction with free electrons in the metal layer. The single solution to resolve such problem is the use of a decreased metal thickness in the OMO configuration by accelerating the formation of a continuous layer. Efforts focused on the synthesis of ultrathin intermediate Ag metal film on chemically heterogeneous oxides have been largely unsuccessful owing to the lack of currently existing methodologies and techniques [23]. Herein, we demonstrate the synthesis of a completely continuous Ag intermediate layer at significantly reduced thicknesses via atomic oxygen-mediated Ag growth to produce OMO TCEs with a ZnO/AgO_x/ZnO structure. This technique improved the likelihood of achieving simultaneously high optical transmittance in the visible range and low electrical resistivity [25–28]. Films composed of ZnO were selected as the top and bottom oxide layers for the OMO structure because of their low cost, non-toxicity, high transmittance, and superior mechanical flexibility compared with ITO electrodes [19,29].

In an OLED device, a significant fraction of the emitted light is internally confined during the outcoupling process because of total internal reflection at the air/substrate and substrate/TCE interfaces, and only a small part of the total emitted light can escape from the light-emitting dielectric medium into the air [30]. This substrate-trapped light loss reduces the eventual throughput and light yield of the OLED device. According to multiple reports, outcoupling can be improved by incorporating a light extracting nanophotonic structures at the air/substrate and ITO/organic layer interface to reduce the refractive index (*n*) difference and create additional light outcoupling routes [31]. For example, a micro-lens array (MLA) [7,32,33], textured surface [34,35], and cylindrical geometry substrate [36] are widely reported to extract light confined in a substrate. In addition, high refractive index substrates [37,38] and light-scattering layers [39–41] that facilitate the extraction of light trapped at TCEs and organic layers have also been studied.

In light of this, we fabricated an antireflection (AR) film comprising silica nanoparticle arrays (SNAs) using a plasma-enhanced chemical vapor deposition (PECVD) technique on polyethylene terephthalate (PET) substrate to further enhance the optoelectronic properties of the OMO structure. An SNA is an ideal candidate for AR film because it can scatter light, suppress reflection from air/substrate interfaces, and enhance light transmission. Furthermore, SNA has a refractive index of ~1.46, which is closer to air (*n* = ~1.0) than the PET substrate (*n* = ~1.58), and the geometrical feature of the AR film implements a nearly complete

suppression of optical reflection in the bottom side of the PET substrate. All these factors are essential to both mitigating waveguided-mode light loss at the air/substrate interface and efficient light outcoupling. The AR film was first prepared on PET substrates using the PECVD to provide light extracting features to the PET substrates without sacrificing optical transparency. The OMO TCEs were fabricated by sequentially depositing ZnO, AgO_x, and ZnO multilayers with different AgO_x intermediate film thickness onto the AR/PET substrate through magnetron sputtering. The optoelectronic properties and device performance of the resulting AR/PET/OMO (AR-OMO) electrode were experimentally and theoretically evaluated.

Fascinatingly, the manipulation of the optical properties of the PET substrate with the simultaneous use of ZnO/AgO_x/ZnO and AR configurations has led to an optical transmittance of 94.2% at 550 nm, which is far superior than any conventional ITO or OMO electrode and is even higher than that of pristine PET substrate without any coating. To the best of our knowledge, this is the highest transmittance value ever reported for PET substrates coated by OMO electrodes. The highly remarkable optoelectronic properties of the AR-OMO TCE also contributed to a significant improvement in the light extraction of the flexible OLEDs, enabling superior luminance efficiency (*LE*) and external quantum efficiency (*EQE*) of the flexible AR-OMO-OLED compared with reference ITO-OLEDs and pristine OMO-OLEDs. The bifunctional AR-OMO electrode-light extractor developed in this work is a low-cost and facile alternative that can replace ITO electrode, which degenerates easily in mechanically flexible optoelectronic applications, such as flexible OLEDs.

2. Experimental section

2.1. Fabrication of the AR film

An SNA-based AR film was fabricated on PET (Panac Co.) substrates 125 μm thick using a custom-built PECVD system at a capacitively coupled radio frequency (RF) discharge of 13.56 MHz, as we demonstrated previously [42–44]. First, the progressive formation of nanoscopic polymer protrusions was induced on the surface of the PET substrate through an argon plasma discharge process conducted at an RF power of 1.1 W/cm² and a working pressure of 220 mTorr. The SNA (with an O:Si atomic ratio of 1.9–2.0) was deposited onto the PET substrate at the same power and working pressure using plasma polymerization of vaporized hexamethyldisiloxane (HMDSO; Sigma-Aldrich, 98% purity) mixed with argon and O₂ gases at a flow rate of HMDSO:O₂:Ar = 1.8: 10: 100 sccm. Both plasma treatment and silica deposition were conducted without intentional heating to avoid thermal damage to the PET.

2.2. Fabrication of AR-OMO TCEs

Transparent ZnO/AgO_x/ZnO OMO TCEs were fabricated by sequentially depositing ZnO, AgO_x, and ZnO multilayers onto the underside of the AR-coated PET substrates using magnetron sputtering (Flexlab System 100; A-Tech System Co. Ltd.) without intentional heating [25]. The bottom (5 nm) and top (25 nm) ZnO films were deposited using a 4-inch ZnO target (99.999% pure ZnO; Applied Science Co.) at an RF power of 200 W and a working pressure of 3.0 mTorr in an argon atmosphere (flow rate = 60 sccm) without heating during and/or after sputtering. Using the same sputtering system, embedded AgO_x layers of different thicknesses (6, 8, and 10 nm) were deposited on the bottom ZnO films via a direct current reactive sputtering process at a power of 50 W using a 4-inch silver target. Deposition of the AgO_x layer was performed

at 3.0 mTorr in an Ar + O₂ atmosphere (Ar:O₂ flow rate = 45:4 sccm). For the fabrication of the reference ITO TCE, an ITO film 160 nm thick was deposited onto the PET substrate using a 4-inch In₂O₃ target doped with 10 wt% tin.

2.3. Fabrication of flexible OLEDs

Flexible OLEDs were fabricated on as-prepared (1) PET/ITO, (2) PET/OMO, and (3) AR/PET/OMO TCE substrates. For fabrication of flexible OLEDs, an ethoxylated polyethyleneimine (PEIE) solution (0.5 wt% in 2-methoxyethanol) was spin-coated onto the TCEs at 5,000 rpm for 30 s to function as an interfacial charge transport layer. The PEIE solution was filtered through a 0.45 μ m polytetrafluoroethylene filter before spin-coating. Next, Super Yellow (PDY-132, Merck) solution (5 mg/mL in toluene) was spin-coated onto the TCE/PEIE substrates at 1,500 rpm for 30 s in an N₂-filled glovebox and postannealed at 70 °C for 20 min to yield an emissive layer 200 nm thick. The samples were then transferred to a high-vacuum ($\sim 10^{-6}$ Torr) chamber, where 10-nm-thick 1,4,5,8,9,11-hexaazatriphenylenehexacarbonitrile (Lumtec) hole injection layer was thermally evaporated at a rate of 0.4–0.5 Å/s. To complete the device fabrication, an aluminum (Al) top anode 100 nm thick was thermally evaporated onto the sample at an evaporation rate of 4–5 Å/s. The light-emission area of each OLED device was fixed at 0.0525 cm².

2.4. Theoretical simulation of AR-OMO TCEs

Rigorous coupled-wave analysis (RCWA) and commercial software (DiffractMOD; RSoft Design Group, USA) were used to calculate the *T* and *R* of the AR-OMO TCEs. In the RCWA, the simulation condition was set to the second diffraction order and a 0.2 nm grid size to calculate the diffraction efficiency, which was enough to numerically stabilize the results. Material dispersions and extinction coefficients were considered for obtaining exact outputs. For the navigation of light rays from the substrate to the air in an emission device, optical simulation based on the Monte Carlo method was carried out using commercial software (Zemax OpticStudio; Radiant Zemax LLC, USA).

2.5. Characterization of AR-OMO TCE-based flexible OLED

Surface morphology and three-dimensional (3D) imaging of the AR/PET substrates were obtained from a field-emission scanning electron microscope (FE-SEM; Hitachi S-4800). The sheet resistance of the OMO TCEs was measured using a non-contact resistance measurement instrument (Napson, EC-80P). The optical properties of the AR-OMO TCEs, including *T*_{total} and reflectance, were measured using ultraviolet (UV)–visible light spectrophotometry (Perkin Elmer, Lambda 750). The optical constants of the AR-OMO TCEs were measured using a spectroscopic ellipsometry. For device characterization, the current density–voltage–luminance (*J*–*V*–*L*) characteristics, *EQE*, electroluminescence (*EL*) spectra, and angle-resolved *EL* intensity of the flexible OLEDs based on the different TCEs were measured using a source measure unit (Keithley 236) and a spectroradiometer (Konta Minolta CS-2000) in ambient environment.

3. Results and discussions

To enhance the performance of flexible OLEDs, it is necessary to develop a bifunctional TCE-light extractor substrate to mitigate light loss because of reflectance at the air/substrate interface and navigate light out from the substrate. This can be realized by the development of the AR-OMO TCE in this work. The fabrication of an AR-OMO TCE is initiated by the deposition of AR film on the PET substrate. Instead of using nano-patterning by photolithography, we introduce a facile and maskless PECVD method for the direct growth of SNA-based AR film on PET substrate. The growth process mainly consisted of two steps: (1) formation of a micro- or nano-sized polymer protrusion array on a PET substrate via argon plasma treatment at 3 min, (2) deposition of silica nanoparticles on the polymeric protrusion array via PECVD. As shown in Fig. 1(a) and (b), the growth of the SNA was initiated on top of the protrusion array, and the morphology of the protrusions array was determined by the duration of the argon plasma irradiation. Prolonged plasma irradiation will cause coalescence of neighboring protrusions and consequently reduce the protrusions density. Because the morphology of a PET substrate is modified via argon plasma treatment, an AR film can be considered the end product of the

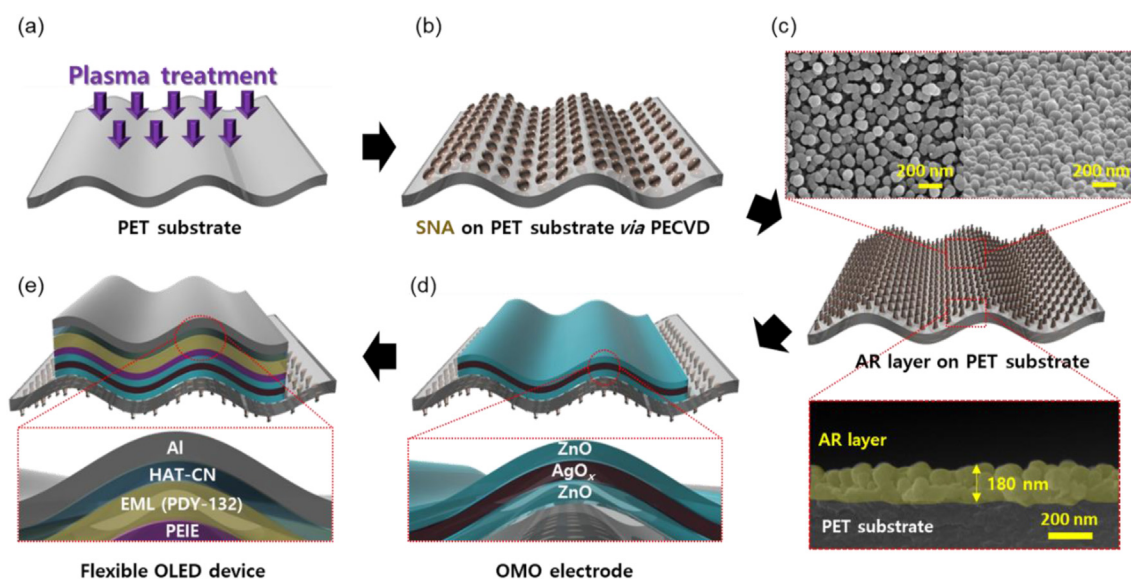


Fig. 1. Schematic fabrication process of SNA-based AR film: (a) formation of nanoscopic polymer protrusions on PET substrate via plasma treatment and (b) deposition of SNA on PET substrate via PECVD technique. (c) Schematic illustration and surface morphology of the as-prepared AR/PET film. Schematic illustration of (d) AR-OMO TCE and (e) flexible yellow-OLED devices based on AR-OMO TCE. (For interpretation of the references to color in this figure legend, the reader is referred to the Web version of this article.)

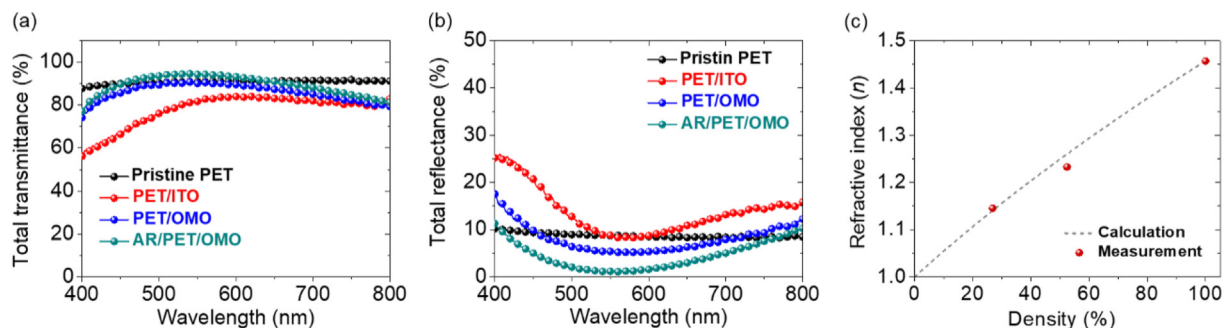


Fig. 2. (a) T_{total} spectra and (b) R_{total} spectra of ITO, OMO and AR-OMO TCEs prepared on PET substrates. (c) Measured/calculated refractive indices (n) of the AR films with different SNA densities.

etching, migration, redeposition, and recombination of the polymer substrate [42]. The top-view and cross-sectional FE-SEM images in Fig. 1(c) depict that the SNA in AR film has an average diameter of ~ 78 nm, and the AR film has an effective thickness of ~ 180 nm. Additional top-view FE-SEM images of the pristine PET substrate and AR/PET film can be found in Fig. S1, Supporting Information. After the preparation of AR film, OMO (ZnO/AgO_x/ZnO) TCE were deposited on the opposite side of the PET substrate via PECVD. The OMO TCE was composed of an AgO_x layer sandwiched between top and bottom ZnO films, as shown in Fig. 1(d). The intermediate AgO_x layer enabled a remarkable degree of enhancement of the optoelectronic properties of the OMO TCE by minimizing the absorption of incident light and carrier scattering [25]. Flexible yellow-OLEDs were then fabricated on the AR-OMO TCE, as can be seen in Fig. 1(e).

We first investigated the optical properties of the as-prepared AR-OMO TCE and compared its performance to pristine OMO and ITO (reference) TCEs. Fig. 2(a) presents the total transmittance (T_{total}) of ITO, OMO, and AR-OMO TCEs deposited on PET substrates in the UV–visible spectral range of 400–800 nm. The recorded T_{total} spectra of the ITO, OMO, and AR-OMO TCEs took into account the background transmittance of PET substrate ($T_{total} > 90\%$ at 400–800 nm). At a wavelength (λ) of 550 nm, the PET/OMO sample exhibited a $T_{550\text{ nm}}$ of $\sim 90\%$, which was much higher than the PET/ITO reference sample $T_{550\text{ nm}}$ of $\sim 82\%$. Further incorporation of AR film enabled an AR/PET/OMO sample to achieve a $T_{550\text{ nm}}$ of $\sim 94\%$, which was 4% higher than that of the PET/OMO analog. Evidently, the simultaneous use of OMO electrode and AR configurations has enabled the AR-OMO TCE to achieve an optical transmittance that is far superior than the ITO or pristine OMO counterparts and is even higher than that of pristine PET substrate without any coating. To the best of our knowledge, this is the highest transmittance value ever reported for PET substrates coated with OMO electrodes reported thus far, as presented in Table S1. In the case of AR/PET/OMO sample, the increase of intermediate AgO_x layer thickness (from 6 to 10 nm) in the OMO structure resulted in a gradual decline of T_{total} , particularly in the λ region of >550 nm region, as can be seen in Fig. S2(a). The total reflectance (R_{total}) values of the ITO, OMO, and AR-OMO deposited on PET substrates are provided in Fig. 2(b). The PET/OMO (without AR film) sample exhibited $\sim 5\%$ lower R_{total} at a wavelength of 550 nm ($R_{550\text{ nm}}$) compared with the PET/ITO sample. The presence of AR film further quenched the $R_{550\text{ nm}}$ of the OMO structure to $\sim 1.2\%$. The reduced reflectance to ambient light in the OMO TCE proved helpful in improving the image contrast of the penultimate OLED device. With increasing AgO_x layer thickness from 6 to 10 nm, there is a corresponding decrease in the $R_{550\text{ nm}}$ value of the AR/PET/OMO sample (Fig. S2(b)), indicating the superior antireflection properties of the intermediate AgO_x layer in the OMO structure. The refractive index and extinction coefficient of

the top and bottom ZnO electrodes and AgO_x interlayer in the OMO structure were also measured and presented in Fig. S3.

Furthermore, the optical properties of the pristine OMO and AR-OMO TCEs were theoretically calculated, and the simulated T_{total} and R_{total} spectra of the pristine OMO and AR-OMO TCEs are presented in Fig. S4. The simulated $T_{550\text{ nm}}$ and the T_{avg} (400–700 nm) of the AR-OMO TCE were recorded at $\sim 75\%$ and $\sim 68\%$, respectively. Pristine OMO TCE (without AR film) exhibited lower simulated $T_{550\text{ nm}}$ ($\sim 69\%$) and T_{avg} (400–700 nm; $\sim 63\%$). The simulated $R_{550\text{ nm}}$ and R_{avg} (400–700 nm) of the AR-OMO TCE were also lower than that of pristine OMO TCE. The measured and simulated optical parameters for the pristine OMO and AR-OMO TCEs are summarized in Table 1. In relation to this, Fig. 2(c) suggests that the refractive indices (n) of the AR film, measured by dividing it into three mediums with different densities, became higher as the density of the silica nanoparticles (SNP) increased. Because of this gradual effective change in n , the measured/simulated T_{total} of the AR-OMO substrate increased marginally with the use of AR film compared with the pristine counterpart. Both experimental and simulated results have coherently confirmed the beneficial use of SNA-based AR film in enhancing the optical properties of the AR-OMO TCE.

To verify the efficacy of ITO, OMO, and AR-OMO TCE substrates in flexible OLED applications, we fabricated ITO-OLED, OMO-OLED, and AR-OMO-OLED devices and evaluated their emission characteristics. Detailed device configuration of the flexible OLED device is illustrated schematically in Fig. 3(a). The thickness of the AgO_x interlayer in OMO-OLED and AR-OMO-OLED was prefixed at 8 nm. Preliminary results obtained during the optimization of AgO_x thickness in OMO structures are presented in Fig. S5 and Table S2. Fig. 3(b) depicts the typical the current density–voltage–luminance (J - V - L) characteristics curves of as-fabricated flexible OLEDs based on different TCEs. There are no significant changes observed in the electrical characteristics of the ITO-OLED and OMO-OLED devices. Dark J - V characteristic curves in Fig. S6 reveal that the OMO-OLED and AR-OMO-OLED exhibited lower leakage current than the ITO-OLED device. Lower leakage current indicates more efficient charge injection and suppressed non-radiative charge recombination in the OLED device

Table 1
Optical properties of ITO-, OMO-, and AR-OMO-coated PET substrates.

Substrate	R_{sheet} ($\Omega/\text{sq.}$)	$T_{550\text{ nm}}$ (%)		T_{avg} (%)		$R_{550\text{ nm}}$ (%)		R_{avg} (%)	
		Exp.	Sim.	Exp.	Sim.	Exp.	Sim.	Exp.	Sim.
PET	—	90.9	—	90.8	—	8.7	—	8.8	—
PET/ITO	32.4	81.7	—	77.9	—	8.8	—	13.7	—
PET/OMO	11.2	90.1	69.1	86.1	62.9	5.4	13.3	8.0	18.0
AR/PET/OMO	11.2	94.2	75.1	89.5	68.4	1.2	5.7	4.4	11.1

Exp, experimental; Sim, simulated.

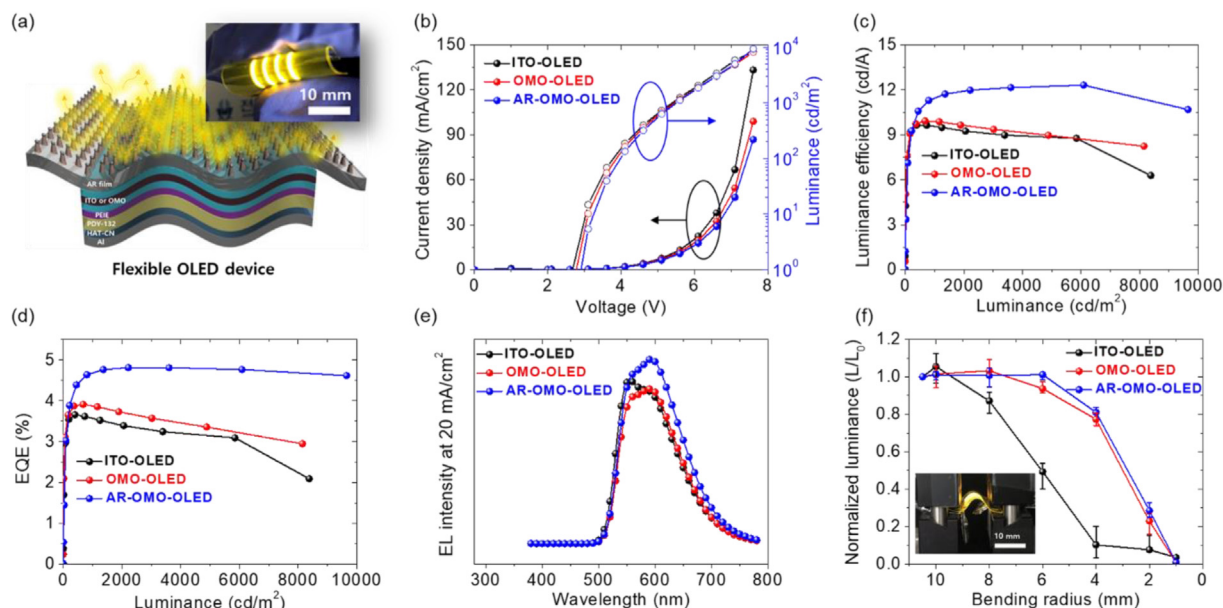


Fig. 3. (a) Schematic device structure of a flexible OLED device using different TCE substrates. (b) J - V - L characteristic curves, (c) LE luminance plots, (d) EQE luminance plots, (e) EL spectra measured at 20 mA/cm^2 , and (f) normalized luminance as a function of r of the flexible ITO-OLED, OMO-OLED, and AR-OMO-OLED devices.

based on the OMO TCEs [45]. Only a minor difference was evident between the electrical characteristic of OMO-OLED and AR-OMO-OLED films. Because the AR film is designed in such a way that it is attached externally to the OLED structure, it had no adverse effect on the device configuration or electrical conductivity of OLED device. However, the introduction of AR film greatly improved the luminance of the OLEDs at the same driving voltage, implying that the AR film was efficiently extracted internally confined photons in the form of a substrate waveguide mode, improving the light out-coupling efficiency [46]. Maximum luminance (L_{max}) values for the ITO-OLED, OMO-OLED, and AR-OMO-OLED were recorded at $\sim 8,300$, $\sim 8,150$, and $\sim 9,400 \text{ cd/m}^2$, respectively. The corresponding LE of the AR-OMO-OLED was much higher than those of the ITO-OLED and OMO-OLED devices, as shown in Fig. 3(c). At $5,000 \text{ cd/m}^2$, the LE values for the ITO-OLED, OMO-OLED, and AR-OMO-OLED devices were 8.8, 8.9, and 12.2 cd/A , respectively. Because of the presence of AR film, the AR-OMO-OLED achieved a maximum LE (LE_{max}) of 12.3 cd/A , which was much higher than that of the ITO-OLED (9.2 cd/A) and OMO-OLED (9.6 cd/A) devices. As a result, the EQE of AR-OMO-OLED reached 4.8%, which was much higher than that of the ITO-OLED (3.7%) and OMO-OLED (3.8%) counterparts, as shown in Fig. 3(d). Fig. 3(e) provides the EL spectra of the OLEDs based on the ITO, OMO, and AR-OMO TCEs at a current density of 20 mA/cm^2 . The EL intensity of the AR-OMO-OLED was apparently higher than the ITO-OLED and OMO-OLED because of the presence of an external AR film that efficiently extracted the light trapped in the substrate waveguide mode.

A bending stability test was conducted to evaluate the mechanical flexibility and robustness of the ITO-OLEDs, OMO-OLEDs, and AR-OMO-OLEDs. The bending stability test was conducted by bending the devices for five cycles at reducing bending radius (r) from 10 mm to 1 mm. As presented in Fig. 3(f), when r was reduced from 10 to 6 mm, only negligible degradation occurred in the normalized luminance (L/L_0) of both the OMO-OLED and AR-OMO-OLED, despite the significant mechanical strain exerted on them. Contrarily, the L/L_0 of the ITO-OLED deteriorated rapidly when r was less than 10 mm, and the disparity between the L/L_0 of the ITO-OLED and AR-OMO-OLED became increasingly larger with

increasingly smaller r . At $r = 4 \text{ mm}$, the OMO-OLED and AR-OMO-OLED retained as much as $\sim 80\%$ of their original luminance, whereas the ITO-OLED suffered 90% loss of luminance. Furthermore, the bending cycle test results (Fig. S7) show the AR-OMO-OLED devices retained $>80\%$ of the initial luminance after being repeatedly bent for 900 cycles at r of 6 mm, confirming that the OMO-structured TCE exhibited a superior mechanical flexibility than the common ITO TCE, and the integration of AR film had no adverse effect on the flexibility of the OLED device.

The total EQE (EQE_{tot}) of the flexible OLED devices based on ITO, OMO, and AR-OMO TCEs was measured with an integrating sphere using a previously described method [6,22], with the results shown in Fig. 4(a). Unlike the calculation of normal EQE , which is based on the collection of light power from a direction normal to the device, the calculation of EQE_{tot} (using an integrating sphere) is based on the collection of all scattered light power in the surroundings [7]. The results reveal that the use of an external AR film produced significantly higher values for EQE_{tot} ($\sim 5.0\%$) in the AR-OMO-OLED ($EQE_{\text{tot}} \sim 5.0\%$), recording 1.31 and 1.25 enhancement ratios relative to the EQE of ITO-OLED ($\sim 3.8\%$) and OMO-OLED ($\sim 4.0\%$), respectively. The device parameters of the flexible OLEDs based on the different TCEs, including turn-on voltage (V_{on}), maximum luminance (L_{max}), LE , EQE , and EQE_{tot} are summarized in Table 2.

To further understand and illustrate the roles of AR film together with OMO structure in the light outcoupling mechanism of an OLED device, a full *trans*-scale optical simulation was conducted using OpticStudio (Zemax Inc.), a commercial 3D optical analysis software based on ray tracing and Monte Carlo methods [36]. The ray-tracing simulation results provided light extraction efficiency, outcoupled power, and angular patterns of the flexible OMO-OLED devices (without AR film) and AR-OMO-OLED devices (with AR film). The amount of light ultimately emitted from the substrate to the air was

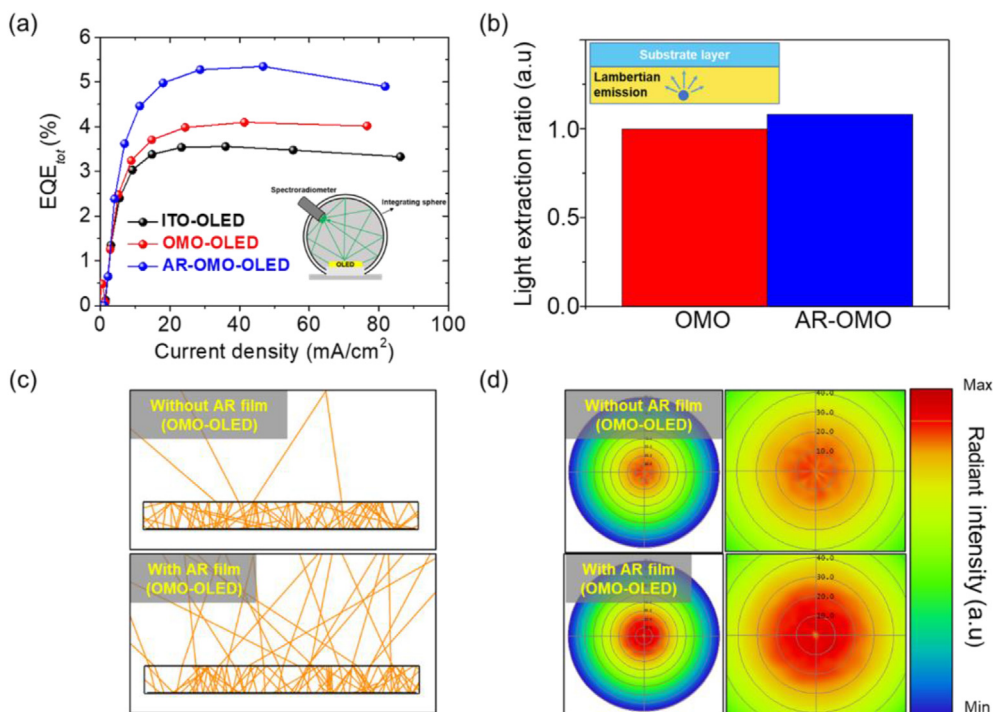


Fig. 4. (a) EQE_{tot} plots of different types of flexible OLEDs measured with an integrating sphere. Ray-tracing simulation outcome: (b) A comparison between the light extraction ratio of flexible OMO-OLED and AR-OMO-OLED structures. (c) Visualization of light navigation pathways for OMO and AR-OMO substrate structure. (d) Radiant intensity contour plots of flexible OMO-OLED and AR-OMO-OLED.

Table 2

Summary of flexible OLED performance.

Devices	V_{on} (V)	L_{max} (cd/m^2)	LE_{max} (cd/A)	EQE (%)	EQE_{tot} (%)
ITO-OLED	2.6 ± 0.1	$8,300 \pm 350$	9.2 ± 0.4	3.7 ± 0.4	3.8 ± 0.3
OMO-OLED	2.7 ± 0.1	$8,150 \pm 450$	9.6 ± 0.2	3.8 ± 0.3	4.0 ± 0.5
AR-OMO-OLED	2.8 ± 0.1	$9,400 \pm 520$	12.3 ± 0.5	4.8 ± 0.4	5.0 ± 0.4

calculated by tracing a total of 10 M rays at wavelength (550 nm). As revealed by the simulation results in Fig. 4(b), the light extraction ratio for an OLED device was improved after applying AR film. Comparatively, the light extraction ratio for the AR-OMO-OLED was ~ 1.08 times greater than that of the OMO-OLED. Fig. 4(c) visualizes the light outcoupling process at the air/substrate interface in the OMO-OLED and AR-OMO-OLED. The simulation results in a dramatic surge in the light navigation pathway of the AR-OMO-OLED because of the suppression of total internal reflection at the air/substrate interface by the AR film. Moreover, the contour plots in Fig. 4(d) reflect the relatively high radiant intensity of the AR-OMO-OLED compared with that of the OMO-OLED. The trends of the simulated results generally agree with the trends from the experimental results, and both experimental and simulated results show that the use of AR film is the main driving factor behind the improvement in emission properties (EQE , EQE_{tot} , and light extraction ratio) of flexible OLED devices.

We then evaluated the device performance of a flexible OLED device in terms of Lambertian emission distribution in a viewing angle range of -70° to 70° . The emission intensity distributions for all of the devices were obtained at a constant luminance of $100 \text{ cd}/\text{m}^2$, with the angular EL profiles depicted in Fig. 5(a). The ITO-OLED device demonstrated poor performance, and Lambertian emission was not achieved. However, both OMO-OLED and AR-OMO-OLED devices produced Lambertian emission with higher EL intensity at larger viewing angles. Among the three devices, the AR-OMO-OLED

exhibited the highest emission at large viewing angle, suggesting that AR film was effective at suppressing surface reflection light loss and optical microcavity effects [48,49]. In the presence of AR film, the flexible OLED device generated more side-direction emissions in the emission intensity distribution pattern. The use of AR film can therefore mitigate emission intensity loss in OLEDs with an increase in viewing angles. The normalized EL intensity in Fig. 5(b) further shows that there is only negligible wavelength shift in the EL of the AR-OMO-OLED with increasing viewing angle. The full width at half maximum (FWHM) of the EL spectra was noticeably reduced with increasing viewing angle, implying that the AR-OMO bifunctional TCE-light extractor helped improve the emission uniformity of the flexible OLEDs at larger viewing angles.

4. Conclusion

We successfully prepared a bifunctional AR-OMO TCE-light extractor layer for a flexible OLED application. Optical properties of AR-OMO TCEs were superior to those of pristine OMO and ITO counterparts, achieving a $T_{550 \text{ nm}}$ of $\sim 94\%$ and a reflectance as low as $\sim 1.2\%$. In the presence of SNA-based AR film, the n difference between the air and the PET substrate was reduced, thereby reducing the substrate waveguided-mode light loss and enhancing the light outcoupling from flexible OLED device. This resulted in superior light-emitting performance in flexible OLED devices. The champion AR-OMO-OLED device achieved an LE of $12.3 \text{ cd}/\text{A}$ and an EQE_{tot} of 5.0% , exceeded the performance of a reference ITO-OLED with a LE of $9.2 \text{ cd}/\text{A}$ and an EQE_{tot} of 3.8% . Furthermore, the flexible OMO-OLED and AR-OMO-OLED also demonstrated much greater mechanical flexibility compared with ITO counterpart, retaining $>95\%$ of their initial luminance under intense bending conditions ($r = 6 \text{ mm}$). The novel design of AR-OMO TCE-light extractor demonstrated herein provides a method to boost the light

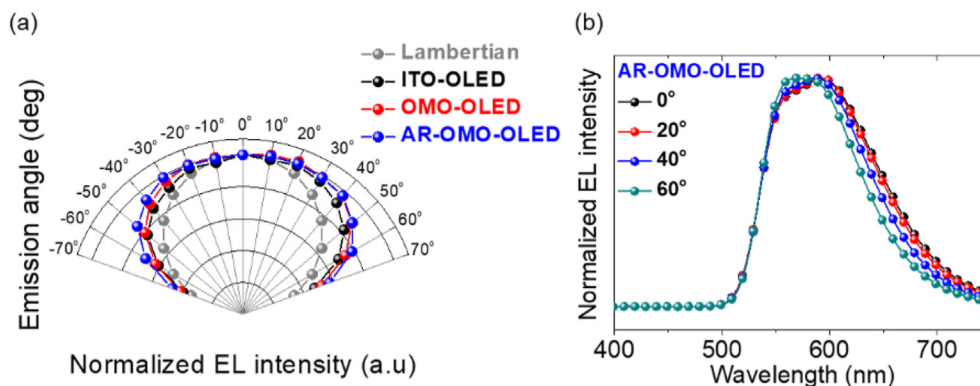


Fig. 5. (a) Angular EL profile of flexible OLEDs based on different TCE structures. (b) Normalized EL spectra of flexible AR-OMO-OLED at different viewing angles.

extraction efficiency of flexible OLEDs without modifying the active layers within the OLED device.

Declaration of competing interest

The authors declare that they have no known competing financial interests or personal relationships that could have appeared to influence the work reported in this paper.

Acknowledgments

This research was financially supported by the Creative Materials Discovery Program (2017M3D1A1039287) and by the Basic Science Research Program (2021R1A2C2004206, 2020R1I1A1A01070661 and 2019R1I1A1A01053127) through the National Research Foundation of Korea (NRF) funded by the Ministry of Education.

Appendix A. Supplementary data

Supplementary data to this article can be found online at <https://doi.org/10.1016/j.mtener.2021.100704>.

References

- [1] M.C. Gather, S. Reineke, Recent advances in light outcoupling from white organic light-emitting diodes, *J. Photon. Energy* 5 (2015), 057607, <https://doi.org/10.1117/1.jpe.5.057607>.
- [2] H.B. Lee, W.Y. Jin, M.M. Ovhal, N. Kumar, J.W. Kang, Flexible transparent conducting electrodes based on metal meshes for organic optoelectronic device applications: a review, *J. Mater. Chem. C* 7 (2019) 1087–1110, <https://doi.org/10.1039/c8tc04423f>.
- [3] A.R. Rathmell, B.J. Wiley, The synthesis and coating of long, thin copper nanowires to make flexible, transparent conducting films on plastic substrates, *Adv. Mater.* 23 (2011) 4798–4803, <https://doi.org/10.1002/adma.201102284>.
- [4] W.-Y. Jin, R.T. Ginting, K.-J. Ko, J.-W. Kang, Ultra-smooth, fully solution-processed large-area transparent conducting electrodes for organic devices, *Sci. Rep.* 6 (2016), <https://doi.org/10.1038/srep36475>.
- [5] J. Liang, L. Li, X. Niu, Z. Yu, Q. Pei, Elastomeric polymer light-emitting devices and displays, *Nat. Photon.* 7 (2013) 817–824, <https://doi.org/10.1038/nphoton.2013.242>.
- [6] S. Park, J.T. Lim, W.Y. Jin, H. Lee, B.H. Kwon, N.S. Cho, J.H. Han, J.W. Kang, S. Yoo, J.I. Lee, Efficient large-area transparent OLEDs based on a laminated top electrode with an embedded auxiliary mesh, *ACS Photonics* 4 (2017) 1114–1122, <https://doi.org/10.1021/acsphotonics.6b00942>.
- [7] S.-R. Shin, H.B. Lee, W.-Y. Jin, K.-J. Ko, S. Park, S. Yoo, J.-W. Kang, Improving light extraction of flexible OLEDs using a mechanically robust Ag mesh/ITO composite electrode and microlens array, *J. Mater. Chem. C* 6 (2018), <https://doi.org/10.1039/c8tc01415a>.
- [8] K.J. Ko, H.B. Lee, J.W. Kang, Flexible, wearable organic light-emitting fibers based on PEDOT:PSS/Ag-fiber embedded hybrid electrodes for large-area textile lighting, *Adv. Mater. Technol.* 5 (2020) 1–8, <https://doi.org/10.1002/admt.202000168>.
- [9] S. Jung, S. Lee, M. Song, D.G. Kim, D.S. You, J.K. Kim, C.S. Kim, T.M. Kim, K.H. Kim, J.J. Kim, J.W. Kang, Extremely flexible transparent conducting electrodes for organic devices, *Adv. Energy Mater.* 4 (2014), <https://doi.org/10.1002/aenm.201300474>.
- [10] D. Zhang, K. Ryu, X. Liu, E. Polikarpov, J. Ly, M.E. Thompson, C. Zhou, Transparent, conductive, and flexible carbon nanotube films and their application in organic light-emitting diodes, *Nano Lett.* 6 (2006) 1880–1886, <https://doi.org/10.1021/nl0608543>.
- [11] J. Li, L. Hu, L. Wang, Y. Zhou, G. Grüner, T.J. Marks, Organic light-emitting diodes having carbon nanotube anodes, *Nano Lett.* 6 (2006) 2472–2477, <https://doi.org/10.1021/nl061616a>.
- [12] G. Gruner, Carbon nanotube films for transparent and plastic electronics, *J. Mater. Chem.* 16 (2006) 3533–3539, <https://doi.org/10.1039/b603821m>.
- [13] J. Lee, T.H. Han, M.H. Park, D.Y. Jung, J. Seo, H.K. Seo, H. Cho, E. Kim, J. Chung, S.Y. Choi, T.S. Kim, T.W. Lee, S. Yoo, Synergetic electrode architecture for efficient graphene-based flexible organic light-emitting diodes, *Nat. Commun.* 7 (2016) 1–9, <https://doi.org/10.1038/ncomms11791>.
- [14] T.H. Han, Y. Lee, M.R. Choi, S.H. Woo, S.H. Bae, B.H. Hong, J.H. Ahn, T.W. Lee, Extremely efficient flexible organic light-emitting diodes with modified graphene anode, *Nat. Photon.* 6 (2012) 105–110, <https://doi.org/10.1038/nphoton.2011.318>.
- [15] J. Wu, M. Agrawal, H.A. Becerril, Z. Bao, Z. Liu, Y. Chen, P. Peumans, Organic light-emitting diodes on solution-processed graphene transparent electrodes, *ACS Nano* 4 (2010) 43–48, <https://doi.org/10.1021/nn900728d>.
- [16] S. Liu, H. Yu, Q. Zhang, F. Qin, X. Zhang, L. Zhang, W. Xie, Efficient ITO-free organic light-emitting devices with dual-functional PSS-rich PEDOT:PSS electrode by enhancing carrier balance, *J. Mater. Chem. C* 7 (2019) 5426–5432, <https://doi.org/10.1039/c9tc00648f>.
- [17] W.H. Kim, A.J. Mäkinen, N. Nikolov, R. Shashidhar, H. Kim, Z.H. Kafafi, Molecular organic light-emitting diodes using highly conducting polymers as anodes, *Appl. Phys. Lett.* 80 (2002) 3844–3846, <https://doi.org/10.1063/1.1480100>.
- [18] M. Kim, C. Lim, D. Jeong, H.S. Nam, J. Kim, J. Lee, Design of a MoO_x/Au/MoO_x transparent electrode for high-performance OLEDs, *Org. Electron.* 36 (2016) 61–67, <https://doi.org/10.1016/j.orgel.2016.05.035>.
- [19] S. Kyu Kang, D. Yun Kang, J. Wan Park, K. Rock Son, T. Geun Kim, Work function-tunable ZnO/Ag/ZnO film as an effective hole injection electrode prepared via nickel doping for thermally activated delayed fluorescence-based flexible blue organic light-emitting diodes, *Appl. Surf. Sci.* 538 (2021) 148202, <https://doi.org/10.1016/j.apsusc.2020.148202>.
- [20] H.W. Lu, C.W. Huang, P.C. Kao, S.Y. Chu, ITO-free organic light-emitting diodes with MoO₃/Al/MoO₃ as semitransparent anode fabricated using thermal deposition method, *Appl. Surf. Sci.* 347 (2015) 116–121, <https://doi.org/10.1016/j.apsusc.2015.03.188>.
- [21] L.P. Ma, W. Ren, H.M. Cheng, Transfer methods of graphene from metal substrates: a review, *Small Methods* 3 (2019) 1–13, <https://doi.org/10.1002/smt.201900049>.
- [22] W. Li, H. Zhang, S. Shi, J. Xu, X. Qin, Q. He, K. Yang, W. Dai, G. Liu, Q. Zhou, H. Yu, S.R.P. Silva, M. Fahlman, Recent progress in silver nanowire networks for flexible organic electronics, *J. Mater. Chem. C* 8 (2020) 4636–4674, <https://doi.org/10.1039/c9tc06865a>.
- [23] S.-R. Park, M.C. Suh, Enhanced device performances of a new inverted top-emitting OLEDs with relatively thick Ag electrode, *Optic Express* 26 (2018) 4979, <https://doi.org/10.1364/oe.26.004979>.
- [24] S.W. Liu, T.H. Su, P.C. Chang, T.H. Yeh, Y.Z. Li, L.J. Huang, Y.H. Chen, C.F. Lin, ITO-free, efficient, and inverted phosphorescent organic light-emitting diodes using a WO₃/Ag/WO₃ multilayer electrode, *Org. Electron.* 31 (2016) 240–246, <https://doi.org/10.1016/j.orgel.2016.01.035>.

- [25] W. Wang, M. Song, T.S. Bae, Y.H. Park, Y.C. Kang, S.G. Lee, S.Y. Kim, D.H. Kim, S. Lee, G. Min, G.H. Lee, J.W. Kang, J. Yun, Transparent ultrathin oxygen-doped silver electrodes for flexible organic solar cells, *Adv. Funct. Mater.* 24 (2014) 1551–1561, <https://doi.org/10.1002/adfm.201301359>.
- [26] J. Yun, W. Wang, T.S. Bae, Y.H. Park, Y.C. Kang, D.H. Kim, S. Lee, G.H. Lee, M. Song, J.W. Kang, Preparation of flexible organic solar cells with highly conductive and transparent metal-oxide multilayer electrodes based on silver oxide, *ACS Appl. Mater. Interfaces* 5 (2013) 9933–9941, <https://doi.org/10.1021/am401845n>.
- [27] G. Zhao, W. Shen, E. Jeong, S.G. Lee, S.M. Yu, T.S. Bae, G.H. Lee, S.Z. Han, J. Tang, E.A. Choi, J. Yun, Ultrathin silver film electrodes with ultralow optical and electrical losses for flexible organic photovoltaics, *ACS Appl. Mater. Interfaces* 10 (2018) 27510–27520, <https://doi.org/10.1021/acsami.8b08578>.
- [28] G. Zhao, E. Jeong, E.A. Choi, S.M. Yu, J.S. Bae, S.G. Lee, S.Z. Han, G.H. Lee, J. Yun, Strategy for improving Ag wetting on oxides: coalescence dynamics versus nucleation density, *Appl. Surf. Sci.* 510 (2020) 145515, <https://doi.org/10.1016/j.apsusc.2020.145515>.
- [29] J.H. Kim, T.W. Kang, S.I. Na, Y.Z. Yoo, T.Y. Seong, ITO-free inverted organic solar cells fabricated with transparent and low resistance ZnO/Ag/ZnO multilayer electrode, *Curr. Appl. Phys.* 15 (2015) 829–832, <https://doi.org/10.1016/j.cap.2015.05.001>.
- [30] Q. Yue, W. Li, F. Kong, K. Li, Enhancing the out-coupling efficiency of organic light-emitting diodes using two-dimensional periodic nanostructures, *Adv. Mater. Sci. Eng.* 12 (2012), <https://doi.org/10.1155/2012/985762>.
- [31] A. Salehi, X. Fu, D.H. Shin, F. So, Recent advances in OLED optical design, *Adv. Funct. Mater.* 29 (2019) 1–21, <https://doi.org/10.1002/adfm.201808803>.
- [32] Y. Ding, Y. Lin, L. Zhao, C. Xue, M. Zhang, Y. Hong, S. Peng, W. Wen, J. Wu, High-throughput and controllable fabrication of soft screen protectors with microlens arrays for light enhancement of OLED displays, *Adv. Mater. Technol.* 5 (2020) 1–9, <https://doi.org/10.1002/admt.202000382>.
- [33] A. Kim, G. Huseynova, J. Lee, J.H. Lee, Enhancement of out-coupling efficiency of flexible organic light-emitting diodes fabricated on an MLA-patterned parylene substrate, *Org. Electron. Phys., Mater. Appl.* 71 (2019) 246–250, <https://doi.org/10.1016/j.orgel.2019.05.025>.
- [34] Y. Han, C.K. Moon, K. Kim, H. Lee, J.J. Kim, Random organic nano-textured microstructures formed by photoexcitation for light extraction of blue OLEDs, *Org. Electron.* 87 (2020) 105892, <https://doi.org/10.1016/j.orgel.2020.105892>.
- [35] B.R. Lee, E.D. Jung, J.S. Park, Y.S. Nam, S.H. Min, B.S. Kim, K.M. Lee, J.R. Jeong, R.H. Friend, J.S. Kim, S.O. Kim, M.H. Song, Highly efficient inverted polymer light-emitting diodes using surface modifications of ZnO layer, *Nat. Commun.* 5 (2014) 1–8, <https://doi.org/10.1038/ncomms5840>.
- [36] K.J. Ko, H.B. Lee, H.M. Kim, G.J. Lee, S.R. Shin, N. Kumar, Y.M. Song, J.W. Kang, High-performance, color-tunable fiber shaped organic light-emitting diodes, *Nanoscale* 10 (2018) 16184–16192, <https://doi.org/10.1039/c8nr05120h>.
- [37] K.-J. Ko, H.B. Lee, M. Jang, M.-H. Lee, J.-W. Kang, Flexible organic light emitting diodes based on bifunctional BaTiO₃ nanoparticles embedded polymer substrate-light extractor, *Mol. Cryst. Liq. Cryst.* 706 (2020), <https://doi.org/10.1080/15421406.2020.1743434>.
- [38] D.W. Kim, J.W. Han, K.T. Lim, Y.H. Kim, Highly enhanced light-outcoupling efficiency in ITO-free organic light-emitting diodes using surface nanostructure embedded high-refractive index polymers, *ACS Appl. Mater. Interfaces* 10 (2018) 985–991, <https://doi.org/10.1021/acsami.7b15345>.
- [39] J. Song, K.H. Kim, E. Kim, C.K. Moon, Y.H. Kim, J.J. Kim, S. Yoo, Lensfree OLEDs with over 50% external quantum efficiency via external scattering and horizontally oriented emitters, *Nat. Commun.* 9 (2018), <https://doi.org/10.1038/s41467-018-05671-x>.
- [40] B.K. Kong, D.H. Kim, T.W. Kim, Significant enhancement of out-coupling efficiency for yarn-based organic light-emitting devices with an organic scattering layer, *Nano Energy* 70 (2020) 104503, <https://doi.org/10.1016/j.nanoen.2020.104503>.
- [41] K. Lee, J.W. Shin, J.H. Park, J. Lee, C.W. Joo, J.I. Lee, D.H. Cho, J.T. Lim, M.C. Oh, B.K. Ju, J. Moon, A light scattering layer for internal light extraction of organic light-emitting diodes based on silver nanowires, *ACS Appl. Mater. Interfaces* 8 (2016) 17409–17415, <https://doi.org/10.1021/acsami.6b02924>.
- [42] E. Jeong, G. Zhao, M. Song, S.M. Yu, J. Rha, J. Shin, Y.R. Cho, J. Yun, Simultaneous improvements in self-cleaning and light-trapping abilities of polymer substrates for flexible organic solar cells, *J. Mater. Chem. A* 6 (2018) 2379–2387, <https://doi.org/10.1039/c7ta09351a>.
- [43] J. Yun, T.S. Bae, J.D. Kwon, S. Lee, G.H. Lee, Antireflective silica nanoparticle array directly deposited on flexible polymer substrates by chemical vapor deposition, *Nanoscale* 4 (2012) 7221–7230, <https://doi.org/10.1039/c2nr32381h>.
- [44] J. Yun, W. Wang, S.M. Kim, T.S. Bae, S. Lee, D. Kim, G.H. Lee, H.S. Lee, M. Song, Light trapping in bendable organic solar cells using silica nanoparticle arrays, *Energy Environ. Sci.* 8 (2015) 932–940, <https://doi.org/10.1039/c4ee01100g>.
- [45] R.K. Hallani, V. Fallah Hamidabadi, A.J. Huckaba, G. Galliani, A. Babaei, M.G. LaPlaca, A. Bahari, I. McCulloch, M.K. Nazeeruddin, M. Sessolo, H.J. Bolink, A new cross-linkable 9,10-diphenylanthracene derivative as a wide bandgap host for solution-processed organic light-emitting diodes, *J. Mater. Chem. C* 6 (2018) 12948–12954, <https://doi.org/10.1039/c8tc05013a>.
- [46] B. Ho, J. Ho, C. Hun, Enhanced light extraction efficiency using self-textured aluminum-doped zinc oxide in organic light-emitting diodes, *Org. Electron.* 51 (2017) 496–500, <https://doi.org/10.1016/j.orgel.2017.09.019>.
- [47] T.H. Han, M.H. Park, S.J. Kwon, S.H. Bae, H.K. Seo, H. Cho, J.H. Ahn, T.W. Lee, Approaching ultimate flexible organic light-emitting diodes using a graphene anode, *NPG Asia Mater.* 8 (2016) 1–8, <https://doi.org/10.1038/am.2016.108>.
- [48] Y.H. Kim, J. Lee, W.M. Kim, C. Fuchs, S. Hofmann, H.W. Chang, M.C. Gather, L. Müller-Meskamp, K. Leo, We want our photons back: simple nanostructures for white organic light-emitting diode outcoupling, *Adv. Funct. Mater.* 24 (2014) 2553–2559, <https://doi.org/10.1002/adfm.201303401>.
- [49] R. Yu, F. Yin, X. Huang, W. Ji, Molding hemispherical microlens arrays on flexible substrates for highly efficient inverted quantum dot light emitting diodes, *J. Mater. Chem. C* 5 (2017) 6682–6687, <https://doi.org/10.1039/c7tc01339f>.